DESIGN OF A UHPFRC USING AMORPHOUS METALLIC FIBRES

Jean Bertrand (1), Anaclet Turatsinze (1), Ahmed Toumi (1) and Florian Bernard (2)

(1) Université de Toulouse, UPS, INSA, LMDC (Laboratoire Matériaux et Durabilité des Constructions), Toulouse, France

(2) Saint Gobain SEVA, Chalon-sur-Saône, France

Abstract

Due to steel fibre corrosion, Ultra High Performance Fibre Reinforced Concrete (UHPFRC) surface may suffer from aesthetic defects. This study addresses the design of an UHPFRC using corrosion-resistant amorphous metallic fibres manufactured by Saint-Gobain SEVA. Workability, compressive, tensile strength and post-cracking behaviour are assessed with regard to the French standard NF P18-470. Moreover, an inverse analysis method is carried out to determine the tensile post-cracking behaviour of the material. With a mixture containing 1% fibre by volume and the most effective polycarboxylate-based superplasticizer among five tested, (a) the workability corresponds to a viscous UHPFRC, (b) the compressive strength corresponds to an UHPFRC 130/145, (c) the tensile strength meets the requirement of the standard, but (d) the criterion of post-cracking energy absorption is not met with 2.34 MPa vs. 3 MPa. Ongoing work in order to optimize the UHPFRC formulation is expected to improve the post-cracking residual strength and fulfill all the requirements of NF P18-470.

Résumé

Le parement d'un BFUP peut présenter des défauts d'aspect dus à la corrosion des fibres d'acier. L'étude s'attache à caractériser un BFUP renforcé par des fibres métalliques amorphes en fabriquées par Saint-Gobain SEVA. L'ouvrabilité, les résistances à la compression et à la traction ainsi que le comportement post-fissuration sont évalués au regard de la norme française NF P18-470. La méthode d'analyse inverse est mise en œuvre pour déterminer le comportement post-fissuration du matériau. Avec 1% de fibres en volume et le plus efficace des superplastifiants à base de polycarboxylates choisi parmi les cinq testés, on obtient (a) l'ouvrabilité d'un BFUP visqueux, (b) la résistance à la compression d'un BFUP 130/145, (c) une résistance à la traction conforme aux exigences de la norme, mais (d) un critère d'absorption d'énergie post-fissuration qui, avec 2.34 MPa, est en deçà des 3 MPa requis. Des travaux en cours d'optimisation de la formulation devraient permettre d'augmenter la résistance résiduelle post-fissuration et d'atteindre les exigences de la norme.

1. INTRODUCTION

UHPFRC reinforced with steel fibres is subject to surface fibre corrosion which, if of no structural consequence, although this point could be discussed on the very long term, is undoubtedly the cause of an aesthetic defect that can be avoided using fully corrosion

resistant Amorphous Metallic Fibres (AMF). However, due to its high specific surface and the resulting high bond with the cement matrix, the effect of AMF reinforcement on the brittleness of cement-based materials is different from conventional steel fibre more particularly with regard to the post-cracking behaviour. Studies on AMF reinforced cement composites exist in the literature, but the behaviour of UHPFRCs with AMF is not well established yet. This study attempts to evaluate the performances of an AMF reinforced UHPFRC with respect to the new French standard NF P18-470 [1] published in July 2016.

2. AMORPHOUS METALLIC FIBRES (AMF)

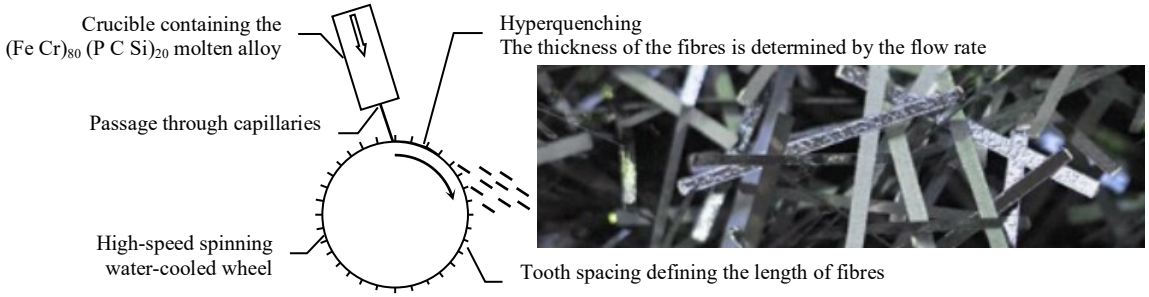

Figure 1: Manufacturing process of amorphous metallic fibres

Conventional steel fibres are made from elongated and thinned wires exhibiting a crystalline structure with preferential directions conferring to the metal anisotropic properties. Amorphous Metallic Fibres (AMF) are manufactured by hyperquenching with a cooling rate above 10^6 K/s (Fig. 1). The melting temperature is therefore passed at such a high rate that the atoms do not have time to form a crystalline array: a supercooled liquid is obtained, which solidifies into an amorphous state where atoms have the disordered isotropic organization of a liquid. The chromium and the isotropy ensure enhanced corrosion resistance and resistance to aggressive agents compared to conventional steel fibres.

AMFs are thinner than the general used short steel fibres (24 or 29 µm vs. 130 µm) and thus exhibit a larger specific area (11.6 kg/m2 vs. 3.9 kg/m2). AMF large specific area, in addition to rough surface of the fibre and high compactness of UHPC matrix result in a very strong bond of AMF to the cement matrix. Therefore AMFs are very efficient in limiting the early opening of the crack, but when the crack opens more widely, the AMF tensile strength is reached before fibres slip. Consequently the toughness, i.e. the resistance to crack opening and propagation, cannot benefit from the part of energy absorption ensured by fibres sliding. AMF scope of use are sanitation networks, road buffers, shotcrete, sealing mortars, technical slabs, prefabrication such as nuclear waste containers, etc. According to the declaration of performance [2], AMFs comply with standard NF EN 14889-1 [3], which makes it possible to use AMFs in accordance with NF P18-470 [1].

3. EXPERIMENTAL PROGRAMME

3.1. Materials and mix proportions

The mix proportions have been defined by Elsa Nguyen Amajean [4] and are presented in Table 1. The cement is supplied by LafargeHolcim-Le Teil plant. Five polycarboxylate-based superplasticizers have been compared. The BASF MasterEase 3700 gives the best results in

terms of flow ability as well as of compressive strength. Its ratio to binder (C+SF) is 4 %. AMFs are incorporated with a volume fraction of 1%. They come in flexible ribbon form (24 μm thick, 1.0 mm wide and 10 mm long), are stainless and exhibit a 1.4 GPa guaranteed and an over 1.8 GPa average tensile strength vs. 2.9 GPa for the general used steel fibres. They are especially convenient in the most aggressive environments. The silica fume to cement ratio (SF/C) is 0.25 and efficient water to binder ratio is 0.218.

Table 1: Mixture proportions of the UHPFRC [values in kg/m^3]

Component	Type	Content
Cement	CEM I 52.5 R	880
Silica fume	95DM supplied by Condensil	220
Sand	0-2 mm	940
Fibres	Fibraflex® FF/10E0 supplied by Saint-Gobain SEVA	72
Efficient water		240
Superplasticizer	MasterEase 3700 supplied by BASF	44

3.2. Mixing procedure

Firstly, dried sand, cement and silica fume are mixed. Then 70% of the water is added and mixed. The rest of the water is then added and mixed with a portion of the superplasticizer to reach a SP/B ratio of 1.60%. Then the rest of the superplasticizer is successively added and mixed, the superplasticizer to binder ratio (SP/B) increasing to 2.40%, 3.00% and eventually 4%. The slump cone test by reference to NF EN 12350-8 [5] is carried out after each addition of superplasticizer, until the flowability of 72 cm corresponding to a viscous UHPFRC is reached.

3.3. Tests

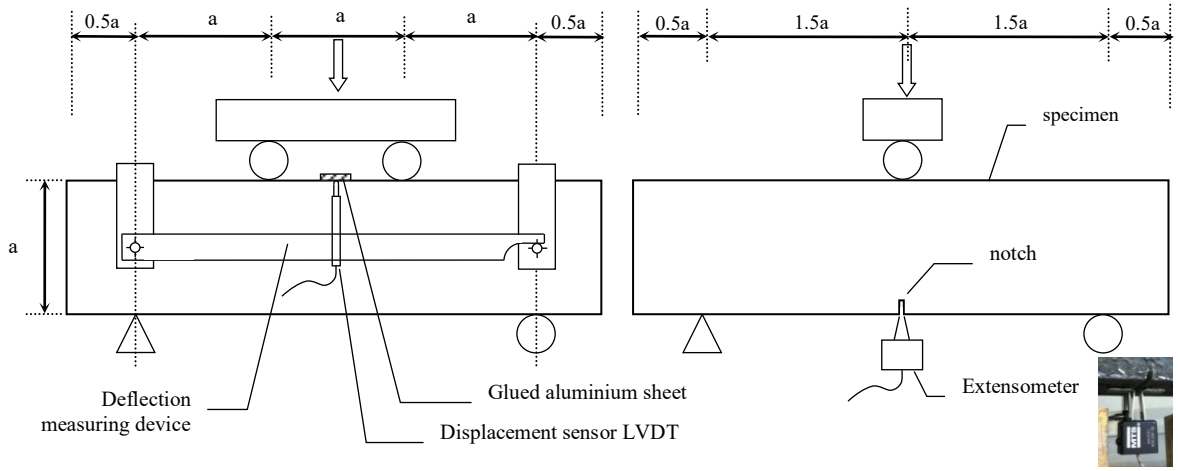

(a) 4-point bending ⇨ $f_{ct,el}$ and E_{cm} (b) 3-point bending ⇨ σ_f-w_{max} law ⇨ Toughness

Figure 2: 4-point bending and 3-point bending experimental set-up

The 28-day compressive strength is determined according to European standard NF EN 12390-3 [6]. 7x7x7 cubes specimens that had been continuously cured at 20 °C and 100% R.H were then tested on a 4000 kN servo hydraulic testing machine. The faces of the specimens were ground to impose high parallelism. The tests were carried out by controlled loading at the rate of 0.5 MPa/s. Three-point and 4-point bending tests were conducted on 28 days cured 7x7x28 cm prismatic specimens (Fig. 2). The bending tests make it possible to evaluate the post cracking tensile behaviour of an UHPFRC, i.e. stress-crack mouth opening law by applying an inverse analysis as detailed in section 4.

4. POST-CRACKING TENSILE BEHAVIOUR AND INVERSE ANALYSIS

The post-cracking tensile behavior of an UHPFRC, i.e. the post-cracking law (stress-crack mouth opening displacement CMOD (σ_f-w_{max})), is determined by the inverse analysis applied to the data from 3-point and 4-point flexure tests (Fig. 2). The inverse analysis is based on the model established by Casanova [7] (Fig. 3) and was developed by Chanvillard [8]. The strain and stress of the cracked section are shown in Fig. 4.

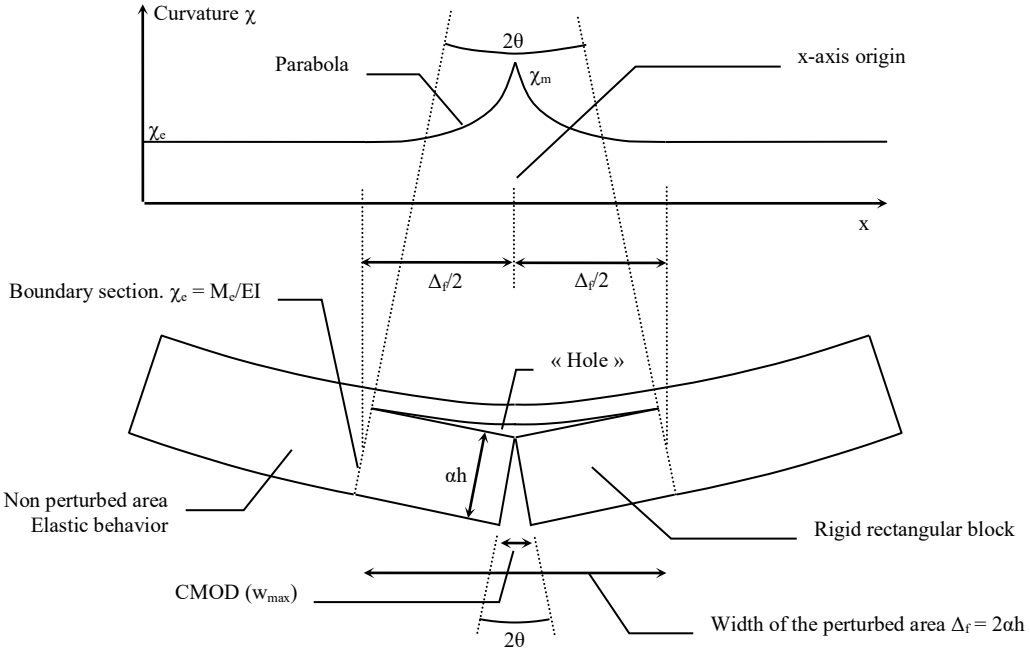

Figure 3: Casanova [7] model of the area around the crack in the case of 4-point bending

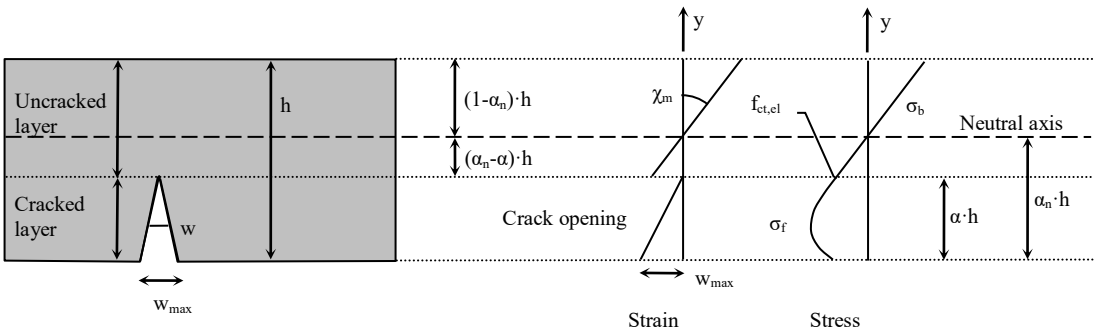

Figure 4: Strain and stress distribution on the cracked section

N , M	Axial force/resisting moment transmitted by the section. $N = 0$
N_b , M_b	Fraction of the axial force/resisting moment transmitted by the uncracked layer
N_f , M_f	Fraction of the axial force/resisting moment transmitted by the cracked layer
b , h	Width and height of the notched section
h_t	Total height of section before notching
α	Relative depth of the crack
α_n	Relative height of the neutral axis
χ_m	Curvature of uncracked layer
M_e	Resisting moment transmitted by the boundary section
χ_e	Boundary section equivalent elastic curvature
$f_{ct,el}$	Tensile limit of elasticity approximated using 4-point bending test
E_{cm}	Young's modulus approximated using 4-point bending test

4.1. Hypotheses

In order to implement the inverse analysis, the five following hypotheses were made:

– **H1**: Two layers are distinguished within the zone perturbed by the crack (Fig. 4): (a) the uncracked upper layer, whose behaviour is in agreement with the strength theory of beams, (b) the cracked lower layer consisting of two rigid rectangular blocks connected by the fibres. This results in a "hole" visible in Fig. 3, which has no physical existence but testifies to the limitations of the model in the very perturbed area surrounding the tip of the crack.

– **H2**: The crack opening w is assumed to be proportional to the distance from the tip of the crack. The relation between the angle θ and the crack opening w_{max} is then, according to Casanova [7]:

$$2\theta = \frac{w_{max}}{\alpha h} \tag{1}$$

– **H3**: The plane sections remain plane, including the upper layer of the cracked section. Consequently, the strain distribution is linear on the upper layer.

– **H4**: The zone perturbed by the presence of the crack extends on either side of the crack over a total width $\Delta f = 2\alpha h$, where αh is the depth of the crack.

– **H5**: The variation of the curvature of the upper layer is assumed to be parabolic from χ_m to χ_e over the distance $\Delta f/2$ which separates the cracked section and the boundary section.

In the rest of this study, the equations whose number is followed by a superscript star are imposed by NF P18-470 [1]. The other equations have been developed by the authors.

4.2. Mechanical balance and expressions of N_f, M_f, N_b and M_b

The mechanical balance of the section leads to the following equations:

$$M = M_b + M_f \tag{2*}$$

$$N = N_b + N_f = 0 \tag{3*}$$

With hypothesis **H2**, the origin of the y-axis taken at the tip of the crack and the moment calculated with respect to the lower fibre, the expressions of N_f and M_f are as follows:

$$N_f = \int_0^{\alpha h} \sigma_f \cdot b \cdot dy = \frac{\alpha \cdot h \cdot b}{w_{max}} \int_0^{w_{max}} \sigma_f \cdot dw \tag{4}$$

$$M_f = \int_0^{\alpha h} \sigma_f \cdot b \cdot dy \cdot (\alpha \cdot h - y) = \alpha \cdot h \cdot N_f - \frac{(\alpha \cdot h)^2 \cdot b}{w_{max}^2} \int_0^{w_{max}} \sigma_f \cdot w \cdot dw \tag{5}$$

The origin of the y-axis is now taken at the neutral axis. Then :

$$N_b = \int_{-(\alpha_n-\alpha)h}^{(1-\alpha_n)h} \sigma_b \cdot b \cdot dy = \int_{-(\alpha_n-\alpha)h}^{(1-\alpha_n)h} E_{cm} \cdot \chi_m \cdot y \cdot b \cdot dy = \frac{E_{cm} \cdot \chi_m \cdot b \cdot h^2}{2} \left[(1-\alpha_n)^2 - (\alpha - \alpha_n)^2 \right] \tag{6}$$

At first, the moment M_b is computed with respect to the neutral axis:

$$M_{b/neutralaxis} = \int_{-(\alpha_n-\alpha)h}^{(1-\alpha_n)h} \sigma_b \cdot b \cdot dy \cdot y = \int_{-(\alpha_n-\alpha)h}^{(1-\alpha_n)h} E_{cm} \cdot \chi_m \cdot y^2 \cdot b \cdot dy = \frac{E_{cm} \cdot \chi_m \cdot b \cdot h^3}{3} \left[(1-\alpha_n)^3 - (\alpha - \alpha_n)^3 \right]$$

The moment M_b computed with respect to the lower fibre is then:

$$M_b = \frac{E_{cm} \cdot \chi_m \cdot b \cdot h^3}{3} \left[(1-\alpha_n)^3 - (\alpha - \alpha_n)^3 \right] + h \cdot \alpha_n \cdot N_b \tag{7*}$$

4.3. Kinematic relationship

The curvatures χ_e and χ_m are linked to the CMOD (w_{max}) through a kinematic relationship proposed by Casanova [7] as a result deduced from the hypotheses **H1** to **H5**. The three following conditions are drawn from hypothesis **H5** and lead to the expression of the curvature:

- Condition 1: For x = 0, the curvature χ is equal to χ_m
- Condition 2: For x = $\Delta f/2$ the curvature χ is equal to χ_e
- Condition 3: The derivative of the curvature is continuous for x = $\Delta f/2$

The angle is then computed as the integral sum of the curvature over the interval [0 ; $\Delta f/2$]:

$$\theta = \frac{\alpha h}{3}(\chi_m + 2\chi_e) \text{ in the case of 4-point bending} \tag{8}$$

$$\theta = \frac{\alpha h}{3}(\chi_m + 2\chi_e) + \frac{M}{3EIL}(\alpha h)^2 \text{ in the case of 3-point bending, with the span L=3a} \tag{9}$$

Considering (1), (8) and (9), the kinematic relationship is as follows:

$$w = \left[\chi_m + 2\chi_e\right]\frac{2\cdot(\alpha\cdot h)^2}{3} \text{ in the case of 4-point bending} \quad (10^*)$$

$$w = \left[\chi_m + 2\chi_e\right]\frac{2\cdot(\alpha\cdot h)^2}{3} + \frac{2\cdot M}{3EIL}(\alpha h)^3 \text{ in the case of 3-point bending} \quad (11)$$

Where the boundary section equivalent elastic curvature is:

$$\chi_e = \frac{12\cdot M_e}{E_{cm}\cdot b\cdot h_t{}^3} \quad (12)$$

Assuming that the crack initiates when the tensile stress in concrete σ_b reaches the tensile limit of elasticity $f_{ct,el}$, the expression of the relative position of the neutral axis is:

$$\alpha_n = \frac{f_{ct,el}}{h\cdot\chi_m\cdot E_{cm}} + \alpha \quad (13^*)$$

4.4. Iterative process

The stress/CMOD law is obtained iteratively by pair of points ($w_{i_{max}}$, σ_{f_i}). In step i, the expression of the axial traction force developed over the height of the crack is given by (4). In step i+1, the load applied to the prism having been slightly increased, the axial load becomes, again in application of (4):

$$N_{fi+1} = \frac{\alpha_{i+1}\cdot h\cdot b}{w_{i+1max}}\int_0^{w_{i+1max}}\sigma_f\cdot dw = \frac{\alpha_{i+1}\cdot h\cdot b}{w_{i+1max}}\int_0^{w_{imax}}\sigma_f\cdot dw + \frac{\alpha_{i+1}\cdot h\cdot b}{w_{i+1max}}\int_{w_{imax}}^{w_{i+1max}}\sigma_f\cdot dw$$

Finally, the expression of $N_{f_{i+1}}$ is:

$$N_{f_{i+1}} = N_{f_i}\cdot\frac{\alpha_{i+1}}{\alpha_i}\cdot\frac{w_i}{w_{i+1}} + \alpha_{i+1}\cdot b\cdot h\cdot\left[\frac{\sigma_{f_i}+\sigma_{f_{i+1}}}{2}\right]\cdot\left[1-\frac{w_i}{w_{i+1}}\right] \quad (14^*)$$

Similarly, the moment $M_{f_{i+1}}$ transmitted over the cracked height in step i+1 is given by (5):

$$M_{f_{i+1}} = \alpha_{i+1}\cdot h\cdot N_{f_{i+1}} - \frac{[\alpha_{i+1}\cdot h]^2\cdot b}{w^2_{i+1max}}\int_0^{w_{i+1max}}\sigma_f\cdot w\cdot dw = \alpha_{i+1}\cdot h\cdot N_{f_{i+1}} - \frac{(\alpha_{i+1}\cdot h)^2\cdot b}{w^2_{i+1max}}\left[\int_0^{w_{imax}}\sigma_f\cdot w\cdot dw + \int_{w_{imax}}^{w_{i+1max}}\sigma_f\cdot w\cdot dw\right]$$

Finally, the expression of $M_{f_{i+1}}$ is:

$$M_{f_{i+1}} = M_{f_i}\cdot\left[\frac{\alpha_{i+1}}{\alpha_i}\cdot\frac{w_i}{w_{i+1}}\right]^2 + \alpha_{i+1}\cdot h\cdot N_{f_{i+1}}\cdot\left[1-\frac{w_i}{w_{i+1}}\right] - \frac{(\alpha_{i+1}\cdot h)^2\cdot b}{2}\cdot\left[1-\frac{w_i}{w_{i+1}}\right]^2\cdot\sigma_{f_{i+1}} \quad (15^*)$$

4.5. Resolution of the system and data filtering

The equations (14*) and (15*) form a system with two unknowns which is solved by expressing $\sigma_{f_{i+1}}$ from (14*). Then (15*) becomes (16), which can be solved by dichotomy to obtain α_{i+1}:

$$0 = M_{b_{i+1}} - M_{i+1} + M_{f_i} \cdot \left[\frac{\alpha_{i+1}}{\alpha_i} \cdot \frac{w_i}{w_{i+1}}\right]^2 + \alpha_{i+1} \cdot h \cdot N_{f_{i+1}} \cdot \left[1 - \frac{w_i}{w_{i+1}}\right] - \frac{(\alpha_{i+1} \cdot h)^2 \cdot b}{2} \cdot \left[1 - \frac{w_i}{w_{i+1}}\right]^2 \cdot \sigma_{f_{i+1}} \quad (16)$$

The offset e of the sensor with respect to the lower fibre must be taken into account in order to obtain the value of the CMOD w_{max}:

$$CMOD = w_{max} = w_{mes} \frac{\alpha h}{\alpha h + e} \quad (17^*)$$

The standard NF P18-470 [1] requires that w_{max} be regularly spaced by 20 µm. The corresponding force is the moving average of the forces recorded over a range of 40 µm centred on w_{max}.

The oscillation of the stress-crack mouth opening (σ_f-w_{max}) relationship is stabilized by applying the following mobile average:

$$\sigma_{fi} = \frac{2\sigma_{fi} + \sigma_{fi+1}}{3} \quad (18^*)$$

Fibres tend to be oriented according to the side of the mould. Besides, in the case of a sawn prism, half of the fibres are considered cut and therefore not anchored. These edge effects are taken into account by dividing the stress σ_{f_i} by a coefficient which is the average of the coefficients presented in Fig. 5 weighted by their area of application.

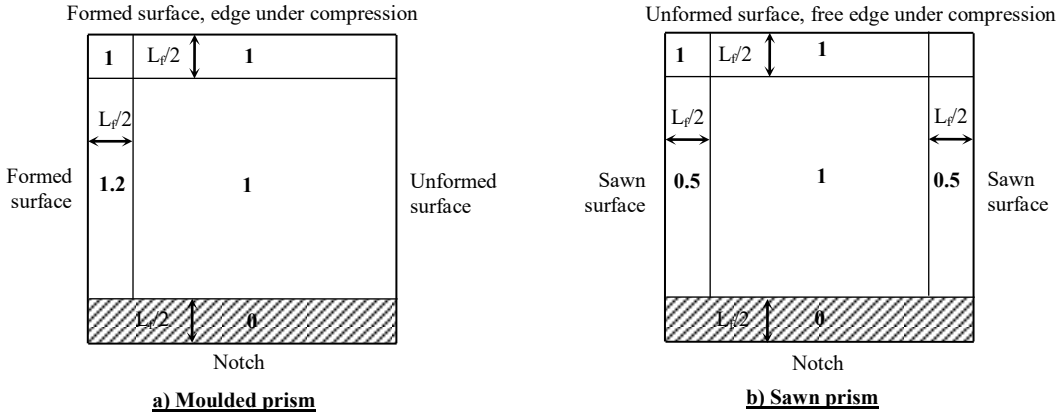

Figure 5: Examples of accounting for edge effects according to NF P 18-470 [1]

5. RESULTS

The average compressive strength is 146 MPa with a maximum strength of 153 MPa, thus possibly meeting the requirement of NF P18-470 [1] for a UHPFRC 130/145.

The tensile limit of elasticity $f_{ct,el}$ and the Young's modulus E_{cm} result from the 4-point bending test: $f_{ct,el}$ = 6.99 MPa and E_{cm} = 34645 MPa. The inverse analysis applied to the results of 3-point bending test on notched prism (Fig. 2b) gives the σ_f-w_{max} law (Fig.6).

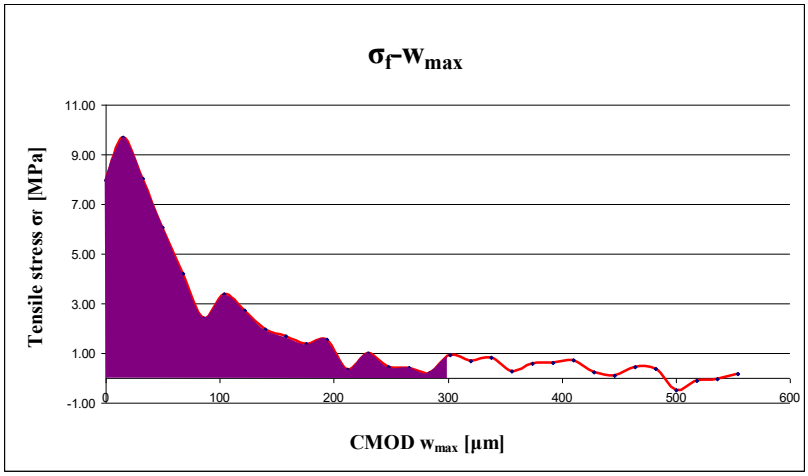

Figure 6: σ_f-w_{max} post-cracking law

The toughness is linked to the area under the σ_f-w_{max} curve, and the UHPFRCs covered by NF P18-470 [1] must have a sufficient strain hardening behaviour under flexure such that they satisfy the following inequality:

$$\frac{1}{w_{0.3}}\int_0^{w_{0.3}} \frac{\sigma_f(w)}{1.25}\,dw \geq \max\left(0.4\cdot f_{ctm,el}\,;3\,\text{MPa}\right) \qquad (19^*)$$

Where:

- $\sigma_f(w)$ is the characteristic post-cracking strength in MPa,
- $w_{0.3}$ = 0.3 mm,
- $f_{ctm,el}$ is the mean value of the limit of elasticity under tension in MPa.

A comparison with the NF P18-470 [1] requirements leads to:

- $f_{ct,el}$ = 6.99 MPa, above the minimum value of 6 MPa imposed by the standard.
- $\frac{1}{w_{0.3}}\int_0^{w_{0.3}} \frac{\sigma(w)}{1.25}\,dw = 2.34\,\text{MPa} < \max\left(0.4\cdot f_{ctm,el}\,;3\,\text{MPa}\right) = 3\,\text{MPa}$, the inequality ($19^*$) is therefore not verified.

6. CONCLUSIONS

Following the tests on the studied UHPFRC with regard to the requirements of NF P18-470, the following observations can be made:

- UHPFRC is a Cv-class, i.e. has a viscous consistence,
- UHPFRC meets the minimum value as regards to tensile limit of elasticity,
- It could be classified as a UHPFRC 130/145 as regards compressive strength,
- UHPFRC does not meet the standard as regards to post-cracking behaviour, with a gap which does not seem insurmountable.

However, this study is a preliminary work which will be pursued by more extensive investigations. The ongoing work aims to design an UHPFRC that would fully meet the requirements of the standard, based on:

- Optimisation of the compactness of the cement-composite,
- Determination of the optimum of AMF length and content,
- Hybrid fibre-reinforcement which remains an alternative to improve again this formulation performances.

In any case, a direct tensile test to validate the result obtained by the inverse method is an exciting objective.

REFERENCES

[1] NF P18-470, 'Concrete – Ultra-high performance fibre-reinforced concrete – Specifications, performance, production and conformity', AFNOR (july 2016).
[2] Saint-Gobain SEVA, 'Declaration of performance concerning Fibraflex metallic fibre', QFA-DDP-FFX-EN Index A, www.fibraflex.com (2016).
[3] NF EN 14889-1, 'Fibres for concrete - Part 1: steel fibres - Definitions, specifications and conformity', AFNOR (2006).
[4] Nguyen Phuong Amanjean, E. 'Développement de Bétons Fibrés Ultra Performants pour la réalisation d'éléments de structure préfabriqués', thèse de Doctorat de l'Université de Toulouse. (2015).
[5] NF EN 12350-8, 'Testing fresh concrete - Part 8: self-compacting concrete - Slump-flow test', AFNOR (2010)
[6] NF EN 12390-3, 'Testing hardened concrete - Part 3: compressive strength of test specimens', AFNOR (2012).
[7] Casanova, P. 'Bétons renforcés de fibres métalliques : du matériau à la structure. Etude expérimentale et analyse du comportement de poutres soumises à la flexion et à l'effort tranchant', in Materials, Ecole Nationale des Ponts et Chaussées. (1995).
[8] Chanvillard, G., 'Caractérisation des performances d'un béton renforcé de fibres à partir d'un essai de flexion. Partie 2 : identification d'une loi de comportement intrinsèque en traction', Materials and Structures 32 (1999) 601-605.